Supporting Information – 10 pages

Ammonolysis with N_2-Diluted NH_3 Suppresses Ta(IV) Defects in $BaTaO_2N$ and Enhances Photocatalytic Water Oxidation

Mahya Salmanion [a], Li Wang [a], Rajesh Kandel [a], Zainab Najaf [a], Guodong Rao [a], William Hahn [a], Klaus van Benthem [a], R. David Britt [a], and Frank E. Osterloh [a]

[a]Department of Chemistry, University of California, Davis, CA 95616, USA

[b]Department of Materials Science and Engineering, University of California, Davis, CA 95616, USA

[c]Department of Metallurgical and Materials Engineering, The University of Alabama, Tuscaloosa, AL, 35401, USA

Email: fosterloh@ucdavis.edu

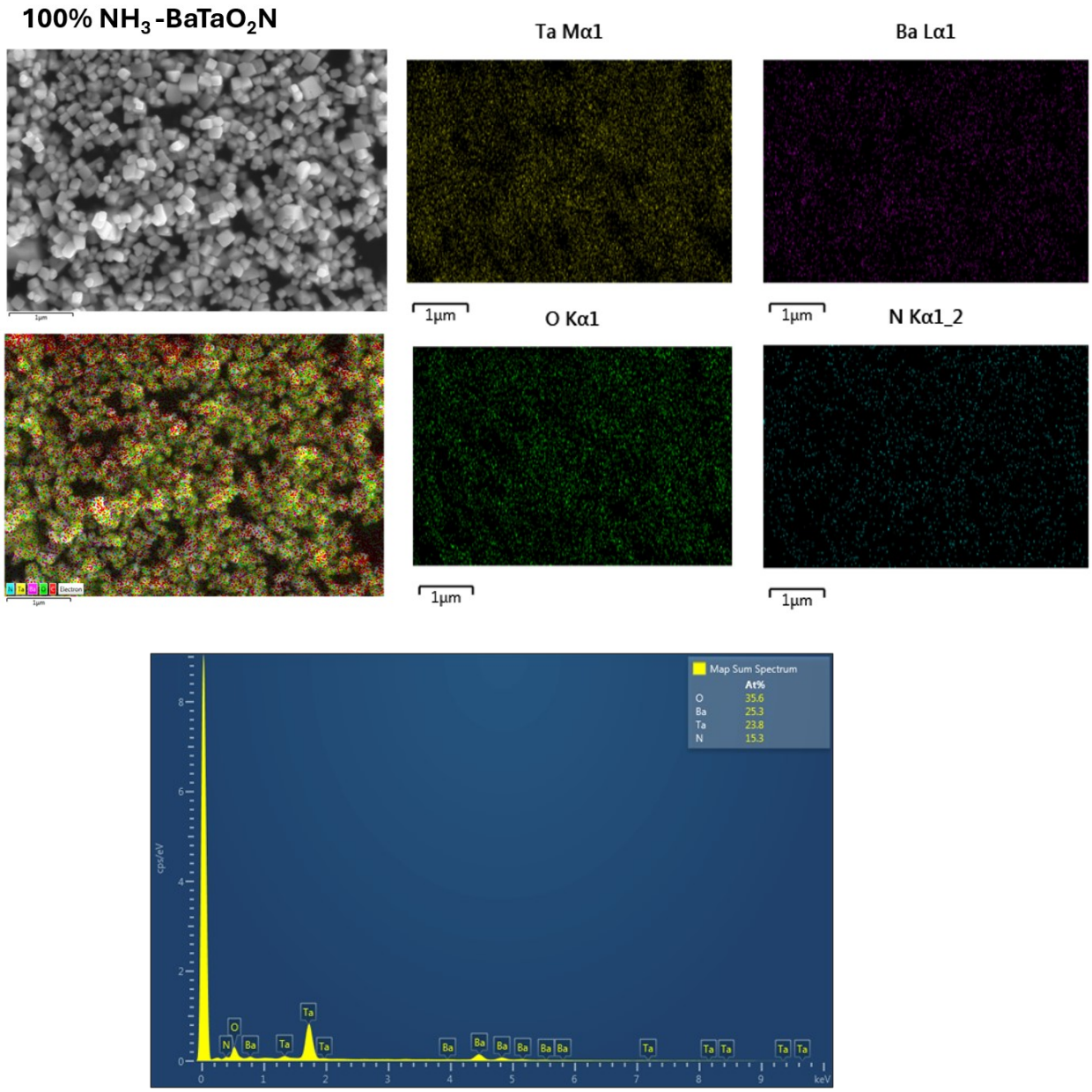

Figure S1. EDX elemental maps of 100% NH_3-$BaTaO_2N$. The overlay image shows the spatial distribution of Ta (cyan), Ba (red), O (green), and N (light blue) on the SEM micrograph. Individual maps confirm the uniform distribution of all elements, including the incorporation of nitrogen. Quantitative EDS results are not reliable for light atoms, such as nitrogen, due to low X-ray yield.

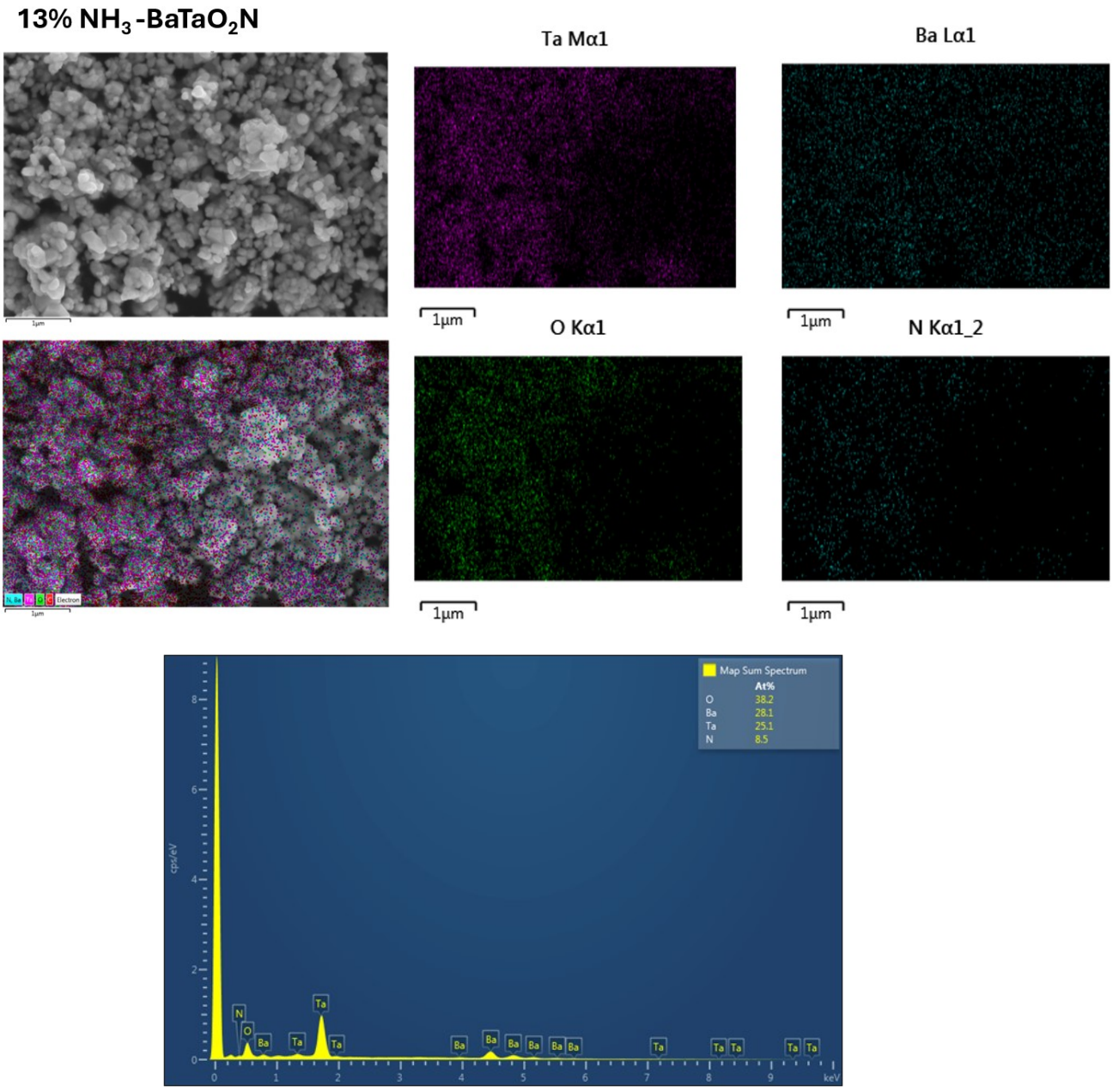

Figure S2. EDX elemental maps of 13% NH_3-$BaTaO_2N$. The overlay and individual maps reveal a uniform and well-dispersed distribution of Ta (magenta), Ba (cyan), O (green), and N (blue) across the surface. Quantitative EDS results are not reliable for light atoms, such as nitrogen, due to low X-ray yield. The lower EDS signal intensity in bottom right is attributed to a shadowing effect.

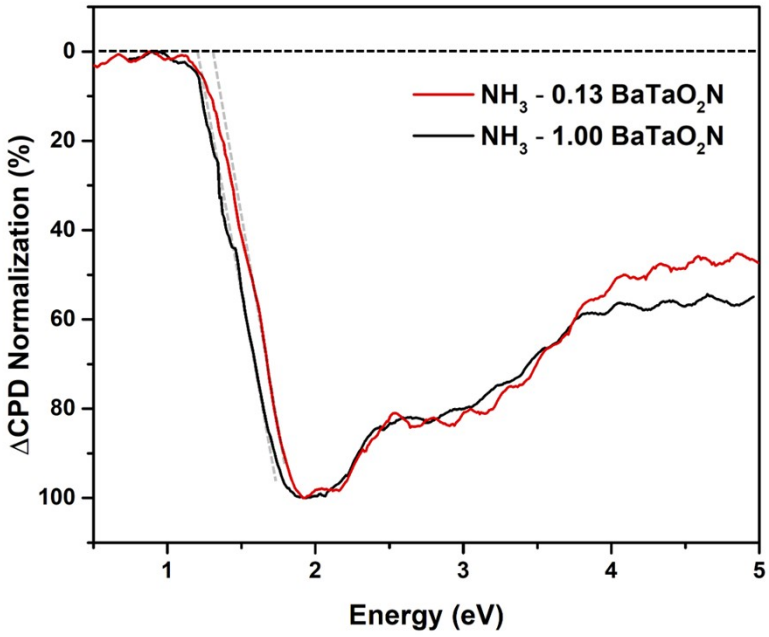

Figure S3. Normalized SPV spectra from **Figure 5**, to reduce the effect of band bending on the SPV signal size. The 0.11 eV SPV blue shift for the 13% NH_3 sample reflects a lower Ta^{4+} defect concentration.

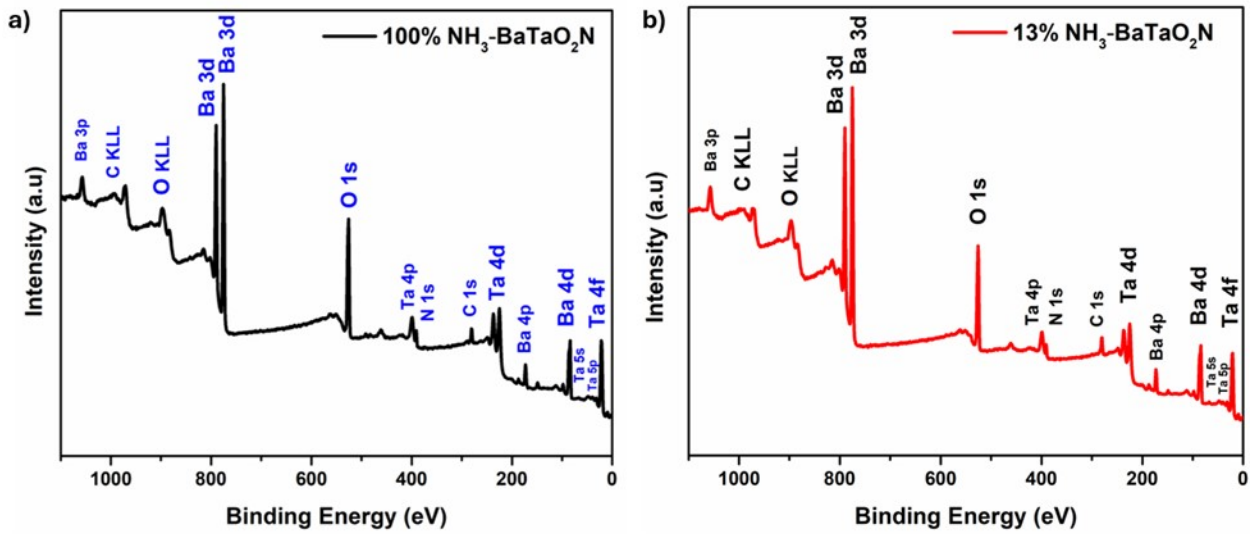

Figure S4. XPS survey spectra of (a) 100% NH_3 and (b) 13% NH_3-synthesized $BaTaO_2N$ samples. Core-level signals corresponding to Ba 3d, Ta 4f, Ta 4d, Ta 4p, O 1s, N 1s confirm the expected elemental compositions. The C 1s peak is from ubiquitous carbon and was used for calibration / charge correction.

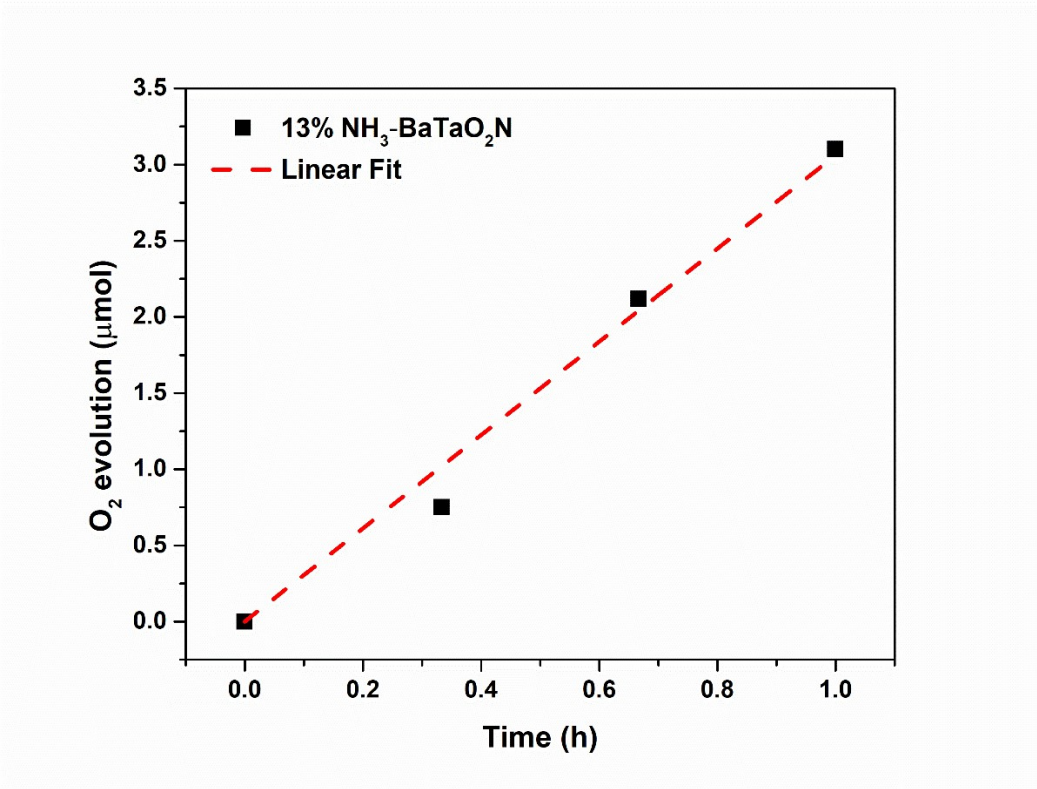

Figure S5. O_2 evolution of 120 mg CoO_x-loaded 13% NH_3-$BaTaO_2N$, measured under a 400 nm LED light in the presence of 0.05 M $AgNO_3$ and 0.2 g of La_2O_3. The linear fit (red dashed line) was used to calculate the apparent quantum efficiency (AQE) of 6.78%.

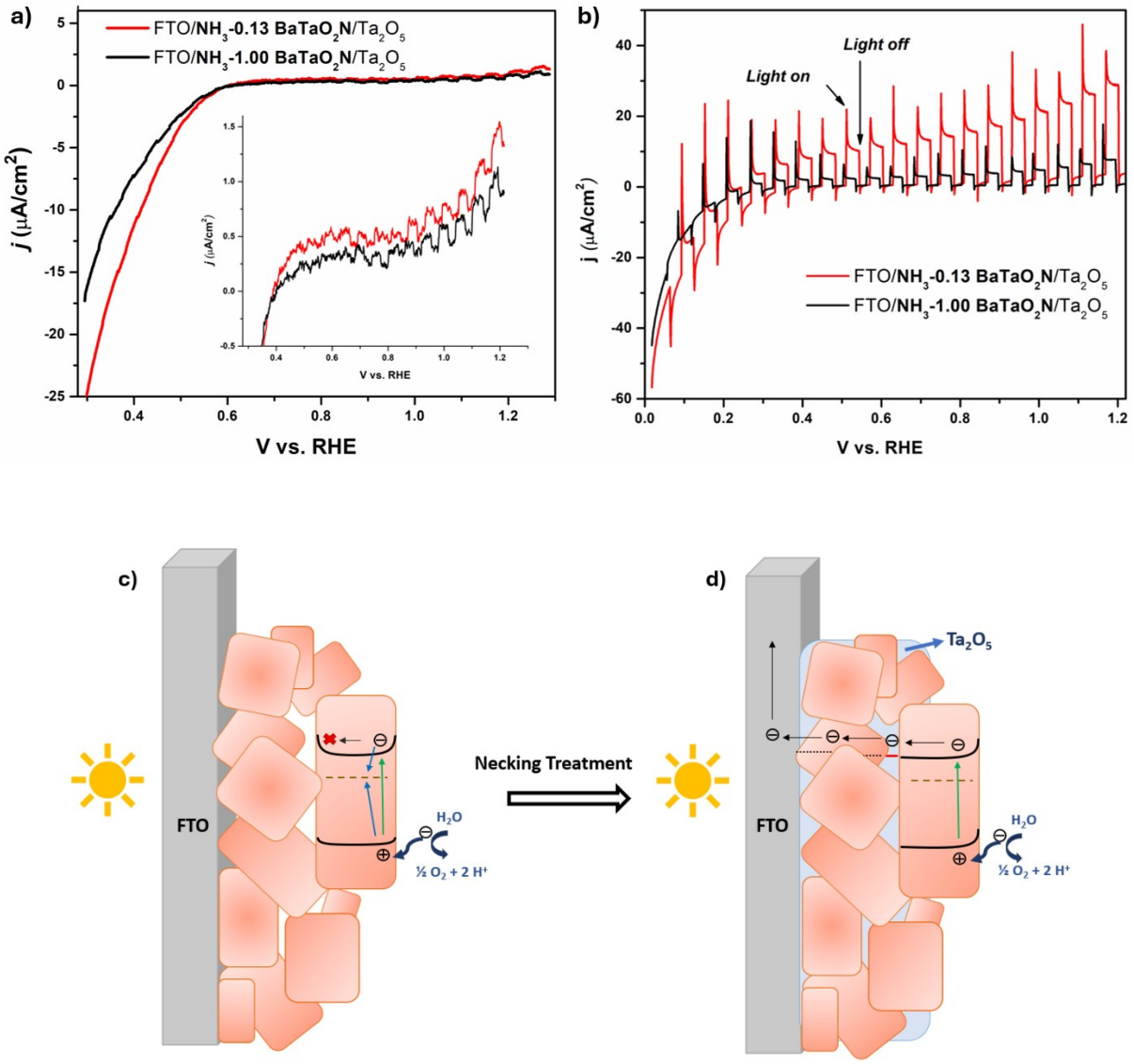

Figure S6. Chopped light linear sweep voltammograms in aqueous 0.5 M Na_2SO_4 solution (pH ≈ 5.75) under intermittent Xe arc lamp irradiation (100 mW cm^{-2}). (a) Electrode without necking (b) with necking treatment (Black for 100% NH_3 and Red 13% NH_3-$BaTaO_2N$). Scan rate: 15 mV sec^{-1} from left to right. Schematic energy diagrams of electrodes before (c) and after (d) necking treatment. The Ta_2O_5 network improves electron transfer in the films.

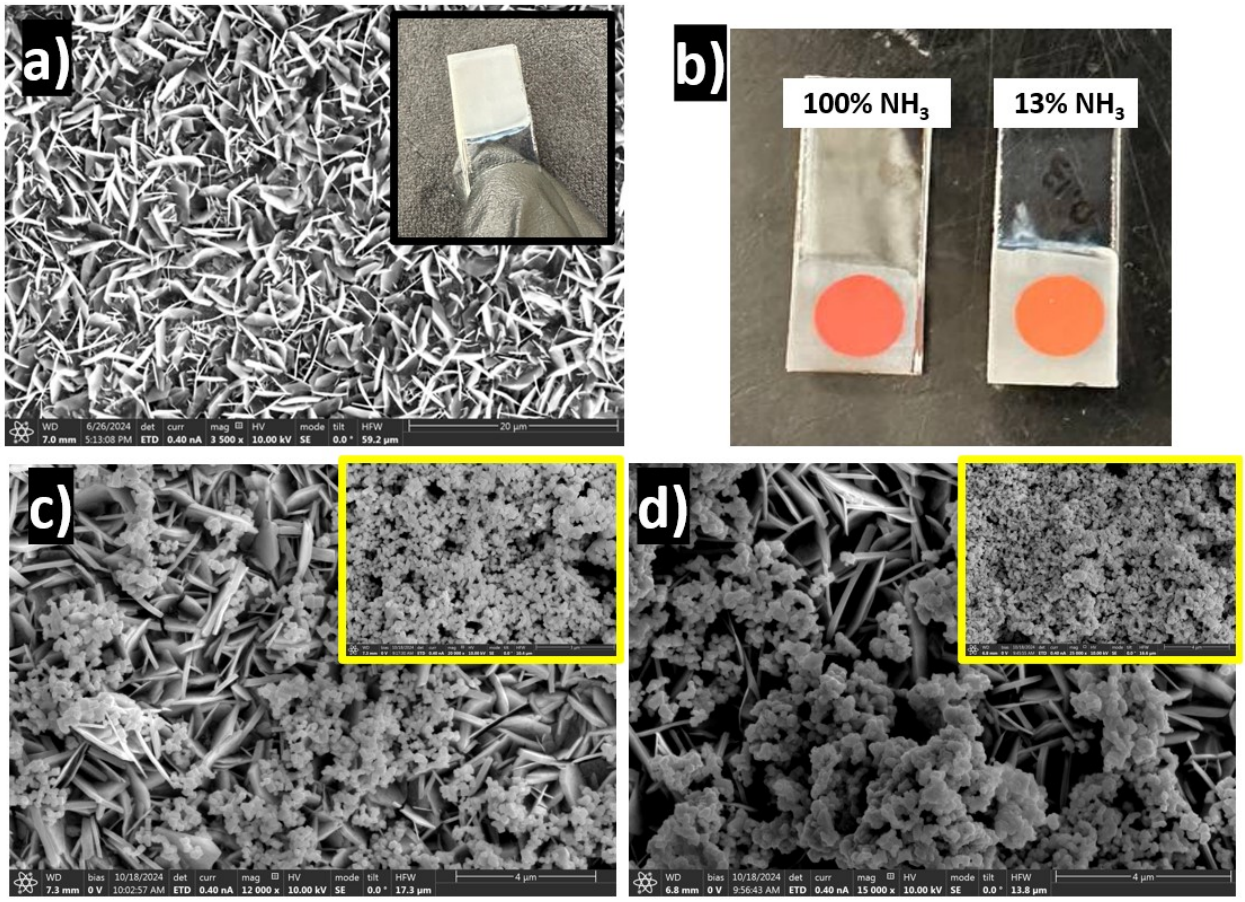

Figure S7. Morphological characterization of ZnO and $BaTaO_2N$-based photoelectrodes. (a) SEM image of electrodeposited ZnO nanostructures on FTO substrate, exhibiting vertically aligned nanoplates. The inset shows a photograph of the freshly prepared ZnO-coated FTO. (b) Photographs of drop-casted $BaTaO_2N$ on ZnO/FTO substrates synthesized in either 100% NH_3 or 13/87% NH_3/N_2 (c,d) SEM images near the electrode edges for (c) 100% NH_3-$BaTaO_2N$ and (d) 13% NH_3-$BaTaO_2N$ samples. Both electrodes show $BaTaO_2N$ particles dispersed over the ZnO surface. Insets in (c) and (d) show top-view SEM images taken from the central area of the respective electrodes, highlighting differences in $BaTaO_2N$ particle morphology.

Table S1. $BaTaO_2N$ photoelectrodes from the literature

Strategy	Photocurrent density at 1.23 V vs RHE	Benefit	Reference
$Co(OH)_x$-FeO_y/$BaTaO_2N$ + particle transfer method	6.5 mA cm^{-2}	Improved interparticle connectivity	[1]
Nanoparticle film on conductive substrate (dual-source electron beam deposition)	4.7 mA/cm^{-2}	Enhanced electron transport	[2]
CoO_x-$BaTaO_2N$/Ta_2N/Ta (RF sputtering and ammonolysis)	4.6 mA cm^{-2}	Conductive Ta_2N interlayer	[3]
Ta_3N_5 NRs / $BaTaO_2N$ core–shell / $FeNiO_x$ cocatalyst	4.5 mA cm^{-2}	Enhanced carrier extraction via Ta_3N_5 nanorods	[4]
Co/$BaTaO_2N$/Ta/Ti + particle transfer method	4.2 mA/cm^{-2}	Improved water oxidation kinetics and charge separation	[5]
CoO_x-$BaTaO_2N$ +particle transfer	3.11 mA cm^{-2}	High surface area and porosity	[6]
CoO microflowers / $BaTaO_2N$ (EPD)	2.05 mA cm^{-2}	CoO collects holes, preventing photocorrosion	[7]
CoPi/TiO_2 /$BaTaO_2N$/Ti (PT method)	1.26 mA cm^{-2}	Transparent/conductive TiO_2 minimizes light shading while boosting active sites	[8]
RhO_x/CoO_x/$BaTaO_2N$/Ti (Electrophoretic deposition and post-necking method)	0.46 mA cm^{-2}	Direct deposition of $BaTaO_2N$ on conductive Ti substrate for better electronic contact and charge transport.	[9]
$BaTaO_2N$ (flux grown) (Particle Transfer Method)	>0.85 mA cm^{-2}	Stable flux-grown crystals with good stability (~35% retained after 24 h)	[10]
IrO_2/TiO_2/$BaZrO_3$-$BaTaO_2N$ (Electrophoretic deposition)	≈0.03 mA cm^{-2}	Overall water splitting under sunlight	[11]
%13 NH_3-$BaTaO_2N$/ZnO/FTO (Drop Casting ; **no Cocatalyst**)	**1.2 mA cm^{-2}**	NH_3 dilution suppresses Ta^{4+} defects.	This work

Table S2. EPR-derived spin and defect parameters of $BaTaO_2N$ samples.

Parameter	**100% NH_3-$BaTaO_2N$**	**13% NH_3-$BaTaO_2N$**
Density of $BaTaO_2N$	8.70 g/cm³	
Molar Mass	364.31 g mol^{-1}	
Ta density	1.44×10^{22} cm^{-3}	
EPR sample mass	4.00×10^{-3} g	
Sample volume	4.60×10^{-4} cm³	
EPR spin amount (obs.)	9.60×10^{-11} mol	–
Unpaired electrons	5.78×10^{13}	–
Spin density	1.26×10^{17} cm^{-3}	1.14×10^{16} cm^{-3}
Ta^{4+} concentration	1.26×10^{17} cm^{-3}	1.14×10^{16} cm^{-3}
Relative EPR signal (to 100% NH_3 sample)	1.00	0.091 (9.1%)

References

1. J. Seo, M. Nakabayashi, T. Hisatomi, N. Shibata, T. Minegishi and K. Domen, *ACS Applied Energy Materials*, 2019, **2**, 5777-5784.
2. X. Luo, Y. Xiao, B. Zhang, C. Feng, Z. Fan and Y. Li, *Journal of Catalysis*, 2022, **411**, 109-115.
3. S. Nishimae, Y. Mishima, H. Nishiyama, Y. Sasaki, M. Nakabayashi, Y. Inoue, M. Katayama and K. Domen, *Solar RRL*, 2020, **4**, 1900542.

4. Y. Pihosh, V. Nandal, T. Minegishi, M. Katayama, T. Yamada, K. Seki, M. Sugiyama and K. Domen, *ACS Energy Letters*, 2020, **5**, 2492-2497.

5. K. Ueda, T. Minegishi, J. Clune, M. Nakabayashi, T. Hisatomi, H. Nishiyama, M. Katayama, N. Shibata, J. Kubota and T. Yamada, *Journal of the American Chemical Society*, 2015, **137**, 2227-2230.

6. M. Hojamberdiev, K. Kawashima, T. Hisatomi, M. Katayama, M. Hasegawa, K. Domen and K. Teshima, *Faraday Discussions*, 2019, **215**, 227-241.

7. S. Wei, S. Chang, F. Yang, Z. Fu, G. Liu and X. Xu, *Chemical Communications*, 2021, **57**, 4412-4415.

8. F. Takagi, S. Taguchi, Y. Kageshima, K. Teshima, K. Domen and H. Nishikiori, *Applied Physics Letters*, 2021, **119**.

9. M. Higashi, K. Domen and R. Abe, *Journal of the American Chemical Society*, 2013, **135**, 10238-10241.

10. M. Hojamberdiev, E. Zahedi, E. Nurlaela, K. Kawashima, K. Yubuta, M. Nakayama, H. Wagata, T. Minegishi, K. Domen and K. Teshima, *Journal of Materials Chemistry A*, 2016, **4**, 12807-12817.

11. K. Maeda and K. Domen, *Angewandte Chemie International Edition*, 2012, **51**, 9865-9869.